remote sensing

MDPI

Article

Accurate Refraction Correction—Assisted Bathymetric Inversion Using ICESat-2 and Multispectral Data

Changda Liu [1], Jiawei Qi [2], Jie Li [1,*], Qiuhua Tang [1], Wenxue Xu [1], Xinghua Zhou [1,3] and Wenjun Meng [1,2]

1 The First Institute of Oceanography, MNR, Qingdao 266061, China; cdliu@fio.org.cn (C.L.); tangqiuhua@fio.org.cn (Q.T.); xuwx@fio.org.cn (W.X.); xhzhou@fio.org.cn (X.Z.); mengwenjun@sdust.edu.cn (W.M.)
2 College of Geodesy and Geomatics, Shandong University of Science and Technology, Qingdao 266590, China; jiaweiqi2019@sdust.edu.cn
3 College of Marine Science and Engineering, Shandong University of Science and Technology, Qingdao 266590, China
* Correspondence: lijie@fio.org.cn

Abstract: Shallow-water depth information is essential for ship navigation and fishery farming. However, the accurate acquisition of shallow-water depth has been a challenge for marine mapping. Combining Ice, Cloud, and Land Elevation Satellite-2 (ICESat-2) bathymetry data with multispectral data, satellite-derived bathymetry is a promising solution through which to obtain bathymetric information quickly and accurately. This study proposes a photon refraction correction method considering sea-surface undulations to address errors in the underwater photons obtained by the ICESat-2. First, the instantaneous sea surface and beam emission angle are integrated to determine the sea-surface incidence angle. Next, the distance of photon propagation in water is determined using sea-surface undulation and Snell's law. Finally, position correction is performed through geometric relationships. The corrected photons were combined with the multispectral data for bathymetric inversion, and a bathymetric map of the Yongle Atoll area was obtained. A bathymetric chart was created using the corrected photons and the multispectral data in the Yongle Atoll. Comparing the results of different refraction correction methods with the data measured shows that the refraction correction method proposed in this paper can effectively correct bathymetry errors: the root mean square error is 1.48 m and the R2 is 0.86.

Keywords: ICESat-2; multispectral data; refraction correction; sea-surface undulations; satellite-derived bathymetry

Citation: Liu, C.; Qi, J.; Li, J.; Tang, Q.; Xu, W.; Zhou, X.; Meng, W. Accurate Refraction Correction—Assisted Bathymetric Inversion Using ICESat-2 and Multispectral Data. *Remote Sens.* **2021**, *13*, 4355. https://doi.org/10.3390/rs13214355

Academic Editors: Peter Romanov and Francesco Serafino

Received: 5 August 2021
Accepted: 26 October 2021
Published: 29 October 2021

1. Introduction

Shallow waters around nearshore environments and islands are closely related to biological survival and human economic activities. Detailed bathymetric data are the basic geographic information necessary to utilize the resources in these areas [1,2]. Therefore, it is necessary to acquire the data on a large scale and with high precision. However, obtaining bathymetry in these regions for marine mapping is difficult. For instance, multibeam and side-scan sonar systems feature poor reachability and narrow bandwidth because of shallow-water depths [3]. Conversely, water depth does not limit the airborne LiDAR bathymetry system [4,5], but its equipment is expensive, and its market penetration rate is low. Moreover, because of its sensor accuracy, the depths obtained by optical remote-sensing bathymetry inversion are limited [1,6,7].

Satellite-derived bathymetry (SDB) is an effective method through which to solve shallow sea bathymetry acquisition. Its physical bases are visible bands that can penetrate the water column [8–11]. There are different methods of SDB determination, which are mainly classified into analytical and empirical models [11]. Empirical modeling, such as the linear function model and the band ratio model, can obtain shallow sea bathymetry using only a small amount of accurate bathymetry data and optical remote-sensing imagery. Lyzenga and Stumpf proposed the classical linear function model and the band ratio model, respectively, which have been widely applied in bathymetry mapping, with promising results [12–14]. However, the empirical model requires a large amount of high-precision bathymetry data to ensure ideal bathymetric inversion results. In previous work, these measured data were obtained from in-situ measurements, which greatly limited the use of this method [15,16].

Adding to the advantages of the SDB method is Ice, Cloud, and Land Elevation Satellite-2 (ICESat-2), which was launched in 2018. ICESat-2 carries the Advanced Topographic Laser Altimeter System (ATLAS), which emits 532-nm blue–green laser pulses with laser beam wavelengths that can penetrate the water body to obtain underwater signals [17–19]. Parrish found that ICESat-2 can perform shallow-water bathymetry. Its laser point cloud penetrates water up to 0.96 Secchi in depth, and the median error of direct measurement is 0.43–0.60 m [20,21].

However, ICESat-2 photon data must also be processed as follows before they can be used. First, ATLAS, a photon-counting lidar carried by ICESat-2, acquires data with high sensitivity. However, this leads to a large amount of noise in the raw data, which seriously affects the representation of valid information [22,23]. Therefore, signal photon extraction must be performed before these data are used. Thus, ICESat-2 features a photon denoising algorithm built into its Level 2 product [18]. The algorithm filters signal photons on the basis of point-cloud density and is more suitable for flat areas [24,25]. For seafloor photons with complex topographies that are affected by scattering from water columns, the denoising results of this method include a significant bias. Second, ICESat-2 Level 2 product data do not consider the effect of water, which results in a position shift of the underwater photons that needs to be carefully corrected. Much work has been carried out by researchers to eliminate the effect. Parrish found that the laser beams emitted by ATLAS were refracted at the air–sea interface. Specifically, the relationship between the angles and the propagation velocity could be derived from Snell's law [20]. In this approach, the sea surface was assumed to be smooth and flat, which ignored the effects of sea surface undulations. Xu found that sea-surface fluctuations affected the distance of penetration of the laser beam in the water, thus affecting the seafloor photon coordinates. Specifically, Xu eliminated the surface undulation error caused by the wave effect by the difference between the water surface and the mean water level [26]. In this method, the laser was assumed to be incident vertically on the sea surface, which ignored the effect of angular variations. Ma believed that the laser beam incidence angle was also affected by the sea-surface slope. However, he neglected that the incident angle of the laser beam was determined by both the slope of the sea surface and the laser transmitting angle [27,28]. Chen proposed an algorithm for refraction correction by tilting the sea level [29]. However, all the above refraction correction models have some limitations, and the bathymetric errors of the laser beam are affected by different effects, such as the sea level variability caused by waves and tides, the refraction effect, and non-nadir incidence, which must be taken into account in a comprehensive manner. Consequently, an effective method is essential to correct the bathymetric information from raw underwater photons.

In this study, combining corrected ICESat-2 lidar datasets and Sentinel-2 imagery, bathymetric maps in shallow waters were produced with only remotely sensed satellite data via the band ratio model. The bathymetric points from the ICESat-2 lidar were used to replace the in-situ bathymetric points. First, an accurate refraction correction method is proposed to obtain high-quality bathymetric photons. In our method, the laser beam incidence angle is determined by both the sea-surface slope and the transmitting zenith angle, and the photon propagation distance in water is related to the instantaneous sea surface and the mean sea surface. In addition, the ICESat-2 bathymetric points after refraction correction are taken as the priori measurements, which are matched with the preprocessed Sentinel-2 multispectral imagery, and the bathymetric maps are generated using the band ratio model in the Yongle Atoll. Finally, the inversion results are compared with the data measured to evaluate the accuracy of the method. The method features low-cost data acquisition and broad coverage, which is a promising solution to balance measurement accuracy, efficiency, and economy.

The content and structure of the paper are organized as follows: Section 2 gives the data and methods of the article. Firstly, the experimental area and data sources are presented in detail; secondly, the steps for the photon refraction correction are derived in detail based on the spatial geometry; finally, the Sentinel-2 data processing and the ratio model are introduced. Section 3 focuses on the experimental results, showing the intermediate results of the experiments as well as the final bathymetric maps and the corresponding error analysis. The discussion is in Section 4, which analyzes in detail the errors affecting the underwater photon positions and the mechanism of each error.

2. Materials and Methods

This study uses ICESat-2 data, Sentinel-2 data, and airborne LiDAR data, which are described in detail in Section 2. Photons that penetrate seawater to reach the seafloor are affected by refraction and sea surface undulations, and do not accurately reflect seafloor topography. Section 2.1 aims to propose an accurate refraction correction method using the spatial geometry of laser beams, which can be used to acquire an accurate seafloor topography. Section 2.2 presents the processing of the Sentinel-2 data, which includes de-glinting and bathymetric inversion models.

The study area covers the Yongle Atoll in the South China Sea (shown in Figure 1), and the water area of this region is about 4 km^2. The South China Sea is the western part of the Pacific Ocean [5,23]. The water depth of the Yongle Atoll area is about 20 m, and it changes slowly with a specific hierarchy. The area is less affected by human activity, and the water is highly transparent, which is typical of these water bodies.

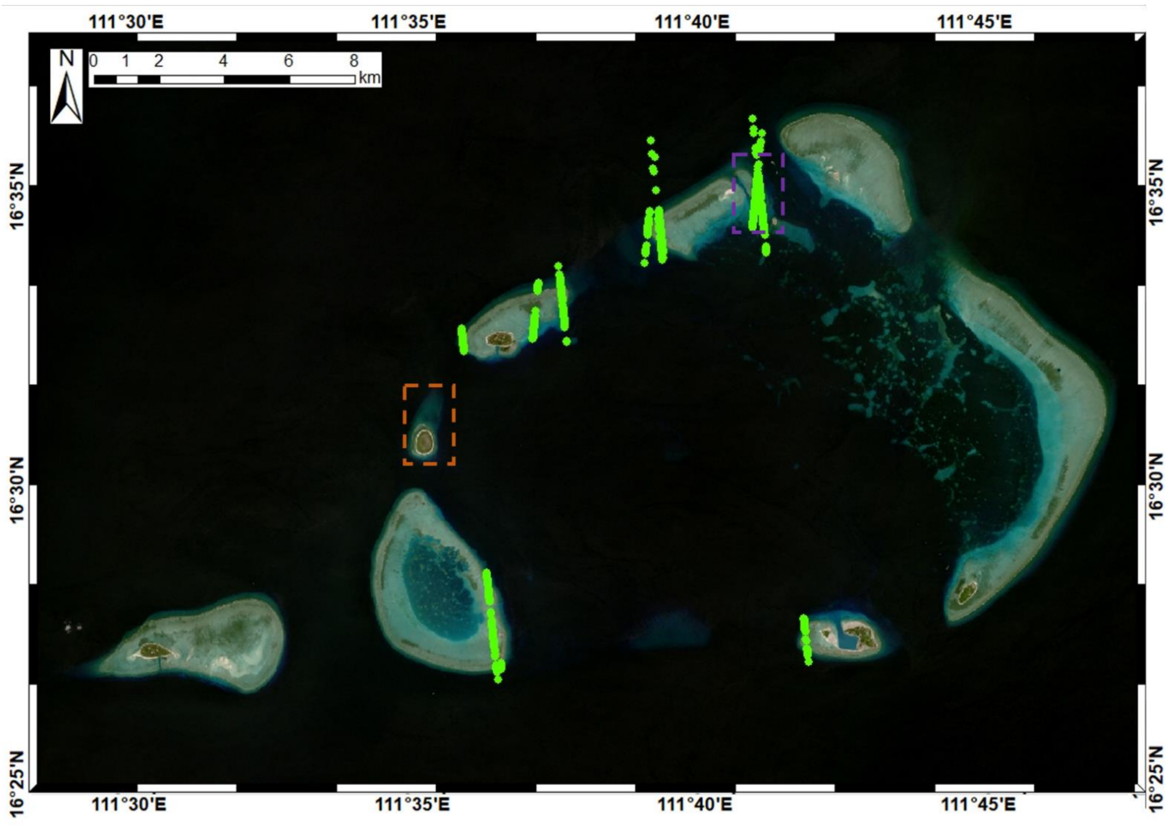

Figure 1. Map of the study area. The background is a remote-sensing image acquired by Sentinel-2 on 24 February 2019. The ICESat-2 passed by the area at GPS time 22 October 2018, 22 February 2019, 12 April 2019, and 19 April 2020. The green points in the figure represent the seafloor signal photon distribution after denoising. The orange box near Ganquan Island illustrates the in-situ measurements (used for validation) and the purple box shows the processing details near Quanfu Island.

The bathymetry of Ganquan Island, the orange boxed area in Figure 1, was measured using an airborne LiDAR bathometer (the Optech Aquarius) in 2012. At the time of measurement, the flight altitude was about 300 m and the point density was 5.5 pts/m^2 [5]. The combined bathymetric accuracy of the dataset is 35 cm and the horizontal positioning accuracy is about 2.5 m. The dataset was resampled to facilitate comparison with later experimental results.

Sentinel-2 is the second satellite operation of the Copernicus Project proposed by the European Space Agency (ESA). It has an orbital altitude of 786 km, an observation width of 290 km, and a 7.25-year lifetime [30]. It consists of two satellites: Sentinel-2A and Sentinel-2B. The revisit period is 10 days for a single satellite and 5 days for an A/B binary satellite. Sentinel-2, which features 13 spectral bands with ground resolutions of 10, 20, and 60 m, carries a multispectral imager (MSI) in push-sweep imaging mode and includes a telescope with an optical pupil diameter of 150 mm. It can perform systematic global land photography and coastal water photography. The spatial resolution of the blue and green bands used for shallow sea bathymetry optical remote-sensing studies is 10 m. Sentinel-2 data are available free of charge to users worldwide from the ESA website (https://scihub.esa.int, accessed on 21 May 2021). This paper used Level 2A products, which were preprocessed through radiometric calibration and atmospheric correction.

ICESat-2, the successor to ICESat, is a lidar satellite launched by the National Aeronautics and Space Administration (NASA) in 2018. ICESat-2 carries an ATLAS sensor that emits single-pulse laser beams at a repetitive frequency of 10 kHz, acquiring photon points at intervals of about 0.7 m in the along-track direction. ATLAS emits a total of six laser beams arranged in three parallel groups, with a spacing of about 3.3 km between groups. Each group contains one strong signal and one weak signal, with an energy ratio of 4:1 [18]. The ICESat-2/ATLAS data are divided into three levels, with 21 standard data products stored in h5 hierarchical files. The data were publicly released in 2019 at the National Snow and Ice Data Center (NSIDC). The ATL03 dataset used in this paper is an ICESat-2 Level 2 product, which contains information on the precise location (i.e., latitude, longitude, and altitude) of photons. Only strong laser beam data are used in this paper to ensure seafloor signal quality.

2.1. ICESat-2 Data Processing

A new photon-counting LIDAR is used in the ICESat-2, whose photomultiplier technology improves detection sensitivity and can achieve photon-level signal detection, improving the detection efficiency significantly. However, this also leads to increased noise and a poor signal-to-noise ratio in the raw data. Therefore, point-cloud denoising is critical. As a result of the limitation of the confidence algorithm used in the ATL03 product, we used the density-based spatial clustering of applications with noise (DBSCAN) algorithm for signal photon extraction, which Martin Ester proposed in 1996 [31]. Ma used a modified DBSCAN algorithm to denoise the ICESat-2 in the South China Sea and near the Gulf of Alaska in the United States and obtained good results. This modified algorithm was used for point-cloud denoising in this paper [27].

The refraction of laser beams at the air–water interface and sea-surface fluctuations can lead to changes in the seafloor photon positions. Considering these factors, we propose a new refraction correction model (Figure 2) to solve the seafloor photon coordinates accurately. Regardless of the error form, it will eventually cause vertical (z-direction) and horizontal (x-direction) changes in the underwater photon positions [32]. Therefore, we interpret the refraction correction model from the perspective of the photon position.

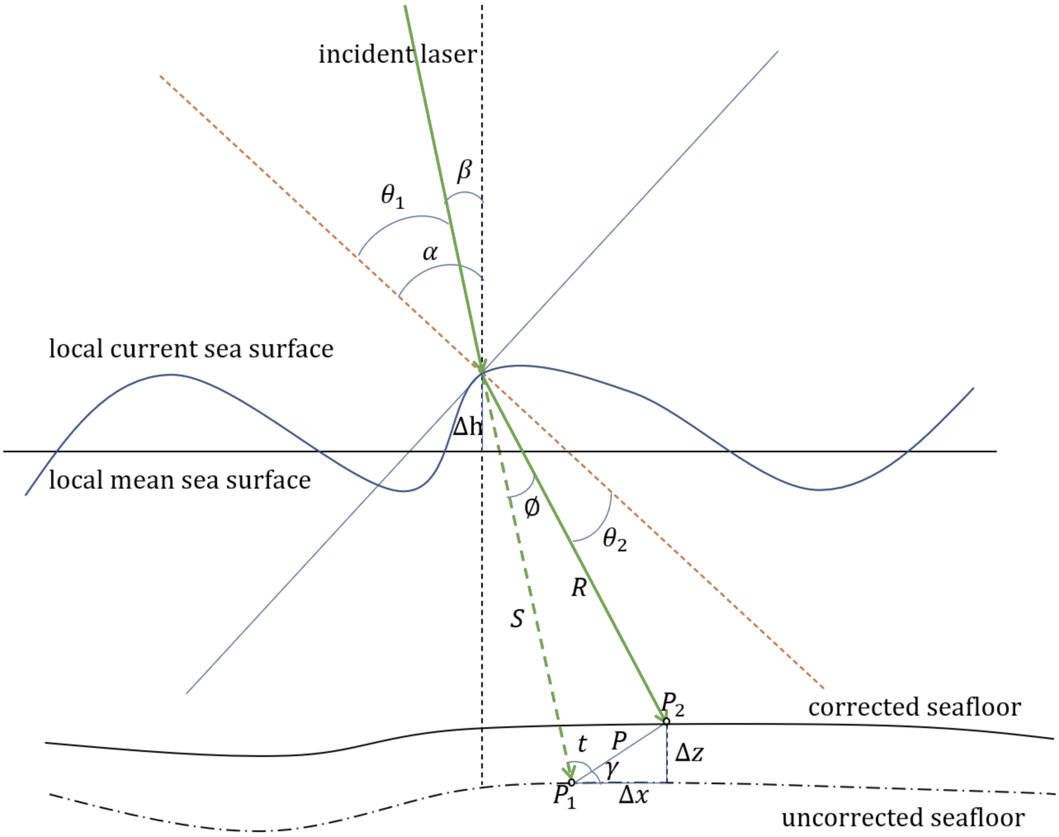

Figure 2. Refraction correction model. The axes in the figure are defined as follows: x is the satellite along-track direction and z is the zenith direction. P_1 and P_2 represent the uncorrected and corrected photon positions, respectively, and O is the incident point. θ_1 and θ_2 refer to the incident and refraction angles, and S and R represent the uncorrected and true propagation distance in water, respectively.

First, we use the concepts of local mean sea level (LM) and sea level undulation (LU). The LM is derived from the mean of high-confidence photons in the local area (1000 m) and illustrates the average height of the local sea level. The LU is derived by fitting surface photons of the same time tag and is used to reflect the current state of the sea level. As a result of the wind, the tide, and other influences, the current surface does not precisely match the local mean surface. The height difference between them is recorded as ΔH, which refers to the wave height. When ΔH is positive, the undulation surface is higher than the local mean surface.

Second, although the DBSCAN algorithm can distinguish signal points and noise points, it cannot add other attribute information into the points [33,34]. Herein, seafloor–surface photon separation must be undertaken before performing photon refraction correction. A proper threshold is key to discriminating between seafloor and surface photons, and an inappropriate threshold would lead to many misclassifications. Ma indicated that all photons with elevations below the local mean sea level minus three times the root mean square wave height are identified as seafloor photons. However, due to the positive wave height, many slightly lower water surface photons may be misclassified. As seafloor photons are involved in the subsequent model training, the misclassification of lower surface photons should receive more attention. Experimental tests found that setting the threshold to the local mean sea level minus five times the root mean square wave height can effectively reduce photon misclassification.

Third, in the refraction correction model proposed by Parrish, the incident angle of the laser beam at the air–seawater interface is only related to the emitted altitude angle. However, there are dynamic fluctuations in the sea surface, and the incident angle is affected by both the altitude angle and sea-surface undulation. Thus, we use the tracking method to correct each seafloor photon position to eliminate these effects as much as possible. In the present model, the difference between the seafloor photons and their corresponding incident points in the along-track direction can be found strictly as $\Delta = -S \cdot \sin\beta$, with β and S representing the emission altitude angle and the uncorrected propagation distance in water, respectively. This overcomes the inability of the photon-counting lidar to obtain the coordinates of the incident points accurately [29]. Generally, β ranges from 0 to 2.0° and is only related to the orbit number. The photons on GT2L and GT2R are almost always emitted vertically, whereas those on the GT1L and GT3R orbits, which are the farthest from the reference orbit, have maximum β [35]. We can derive the sea-surface slope α and the wave height ΔH in the along-track direction based on the current sea surface. The photon incidence angle θ_1 can be expressed as:

$$\theta_1 = \alpha - \beta \tag{1}$$

When the wavelength is 540 nm, the refractive index of seawater is 1.341, with a 35-PSU salinity, 20 °C temperature, and atmospheric pressure. These values are taken as the default settings for n_2 in seawater. Meanwhile, the refractive index of air, n_1, is 1. The refraction angle of seafloor photons can be expressed as:

$$n_1 \sin\theta_1 = n_2 \sin\theta_2 \tag{2}$$

The refraction coefficient leads to variations in the refraction angle and the propagation speed of the laser. For seafloor photons with a distance S not considering the change in propagation speed, the true propagation distance R should be:

$$R = S\frac{n_1}{n_2} \tag{3}$$

In the triangle OP_1P_2, according to the cosine theorem and simple geometric relationships, the following equations are obtained:

$$P = \sqrt{S^2 + R^2 - 2SR\cos(\alpha - \beta - \theta_2)} \tag{4}$$

Furthermore, using the cosine theorem and the relationship between the exterior angles of the triangle, we can obtain

$$\cos t = \frac{S^2 + P^2 - R^2}{2SP} \tag{5}$$

$$\gamma = \frac{\pi}{2} + \beta - t \tag{6}$$

Finally, the vector (Δx, Δz) between the original position P_1 and the corrected position P_2 of the seafloor photon can be solved critically:

$$\Delta z = P\sin\gamma \tag{7}$$

$$\Delta x = P\cos\gamma \tag{8}$$

We found that the seafloor photons feature different numbers of corrections in the x and z directions, and the different errors have different effects on the photon positions. A specific quantitative description is shown in Section 4.1.

Tidal correction is a necessary technical aspect of bathymetric remote-sensing inversion. Performing tidal correction can eliminate inconsistent data acquisition time errors and attribute the results to a uniform depth datum. This paper uses the TMD tidal model for tidal correction presented in Table 1, and all the SDB results after tidal correction are based on the mean sea level [36].

Table 1. Detailed information on acquisition dates and tidal correction results. The ICESat-2 satellite passed over the study area four times.

Data	Acquisition Time	Tide Height (cm)
Sentinel-2	24 February 2019 03:11:16	0.04
ICESat-2	22 October 2018 15:38:35	12.52
ICESat-2	22 February 2019 21:51:59	−42.79
ICESat-2	21 April 2019 06:58:16	6.52
ICESat-2	19 April 2020 13:37:23	17.9

2.2. Sentinel-2 Data Processing

The Sentinel-2 Level 2A product comprises bottom-of-atmosphere-corrected reflectance data that are radiometrically calibrated and atmospherically corrected. De-glinting is required before these data can be used. A glint is a white streak along the edge of a wave on the windward side of the nearshore environment and is typically seen as a very bright spot on remote-sensing images. The method used in this paper was proposed by Hedley, who found that the Fresnel reflections of water bodies are wavelength-independent. The distribution of flares in the near-infrared band is linearly correlated with that in the visible band [37].

In this study, because of its historical significance, simplicity, widespread utilization, and good accuracy, we applied a classical empirical model, the log-ratio model (LRM), to the Sentinel-2 MSI imagery. Using the preprocessed Sentinel-2 images with multiple bands and the ICESat-2 bathymetric points (which were used as prior measurements to calculate the relationship), the LRM was applied to generate the bathymetric map.

Stumpf proposed the classical SDB method in 2003, linking the above-water surface remote-sensing reflectance ratio of blue and green bands to water depths [14]. The log-transformed relationship between the ratio of a higher-absorption band and that of a lower-absorption band was derived. Subsequently, a linear model can be developed using this ratio and the retrievable bathymetry. This model can be expressed as follows:

$$Z = m_1 * \frac{\ln(n * R(\lambda_1))}{\ln(n * R(\lambda_2))} - m_0 \tag{9}$$

where n, m_1, and m_0 are the empirical parameters; Z represents the water depth. Traditionally, $R(\lambda_1)$ and $R(\lambda_2)$ correspond to the reflectance of the blue and green bands, respectively. The empirical parameters are usually calibrated using in-situ bathymetric data.

3. Results

In this section, we present the results obtained using the methods and data described above. Section 3.1 illustrates the results of ICESat-2 after modified DBSCAN algorithm filtering and refraction correction [27]. Section 3.2 demonstrates the results of the Sentinel-2 de-glinting imaging, from which bathymetric data can be obtained. Section 3.3 shows the bathymetric inversion results of the Yongle Atoll and the error comparison results with the in-situ data near Ganquan Island.

3.1. Correction Results of ICESat-2

Figure 3 presents the results of the denoising using the DBSCAN algorithm. We established the coordinate system to better display the detailed processing results, which features the x-axis as the satellite along-track direction and the z-axis as the zenith direction. The x-axis value is calculated from the aircraft velocity and photon time tag, whereas the z-axis value corresponds to the photon WGS84 height. ICESat-2 acquired a large mass of seafloor signals while passing through the middle area between Quanfu Island and Yinyu Island (Figure 3a, corresponding to the purple area in Figure 1); the point-cloud denoising results of this area are shown in Figure 3b. In Figure 3b, by comparing the high-confidence photon points (blue circle points) with the algorithm signal points (green points), we found that the DBSCAN algorithm can effectively extract the seafloor signals.

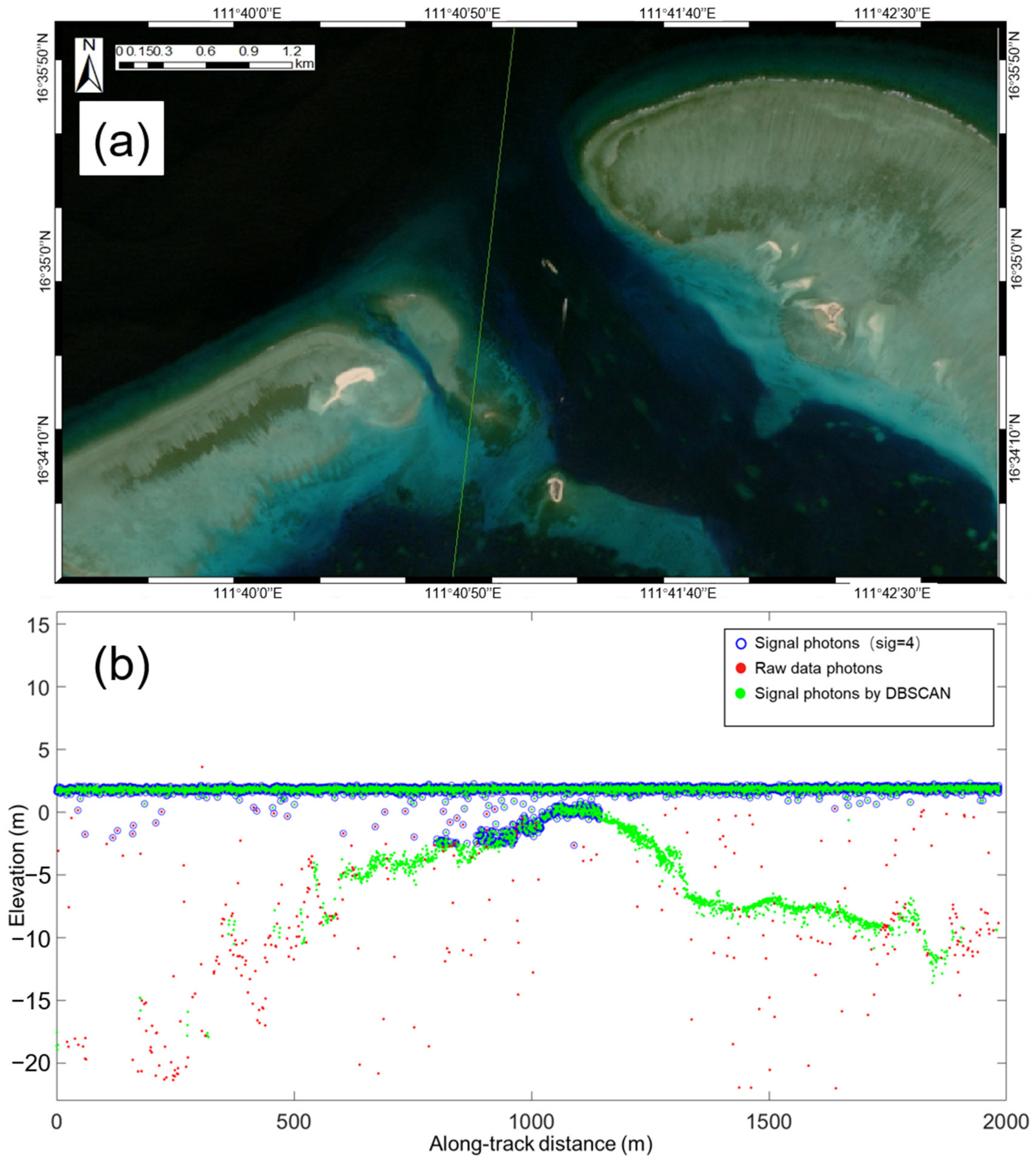

Figure 3. The area between Quanfu Island and Yinyu Island. (**a**) shows the ICESat-2 trajectory using a green line. (**b**) explains the denoising results of the DBSCAN algorithm, in which the green and red points represent the signal and noise, respectively; the points with blue circles represent the high-confidence photons.

Figure 4 shows the results of the seafloor photon refraction correction. As a result of the reset of the seafloor–surface photon separation threshold, a few surface photons were misclassified as seafloor photons. The green dots represent the corrected underwater photon positions and the red dots are the original photon positions. Figure 4a,b show the results of photon correction using Parrish's algorithm and Ma's algorithm, respectively [20,27]. Parrish treated the sea surface as a horizontal plane and considered the seafloor photon position related to the laser beam's refraction at the air–water interface. Ma corrected the underwater photon propagation distance using the sea-surface undulation and equated the incident angle to the mean sea surface slope. In this region, the maximum depth obtained by the ICESat-2 was about 18.5 m, the mean value of sea-surface fluctuation was 0.18 m, and the mean value of sea-surface slope was 8.2°. Figure 4c shows the results of the refraction correction in Section 2.1.

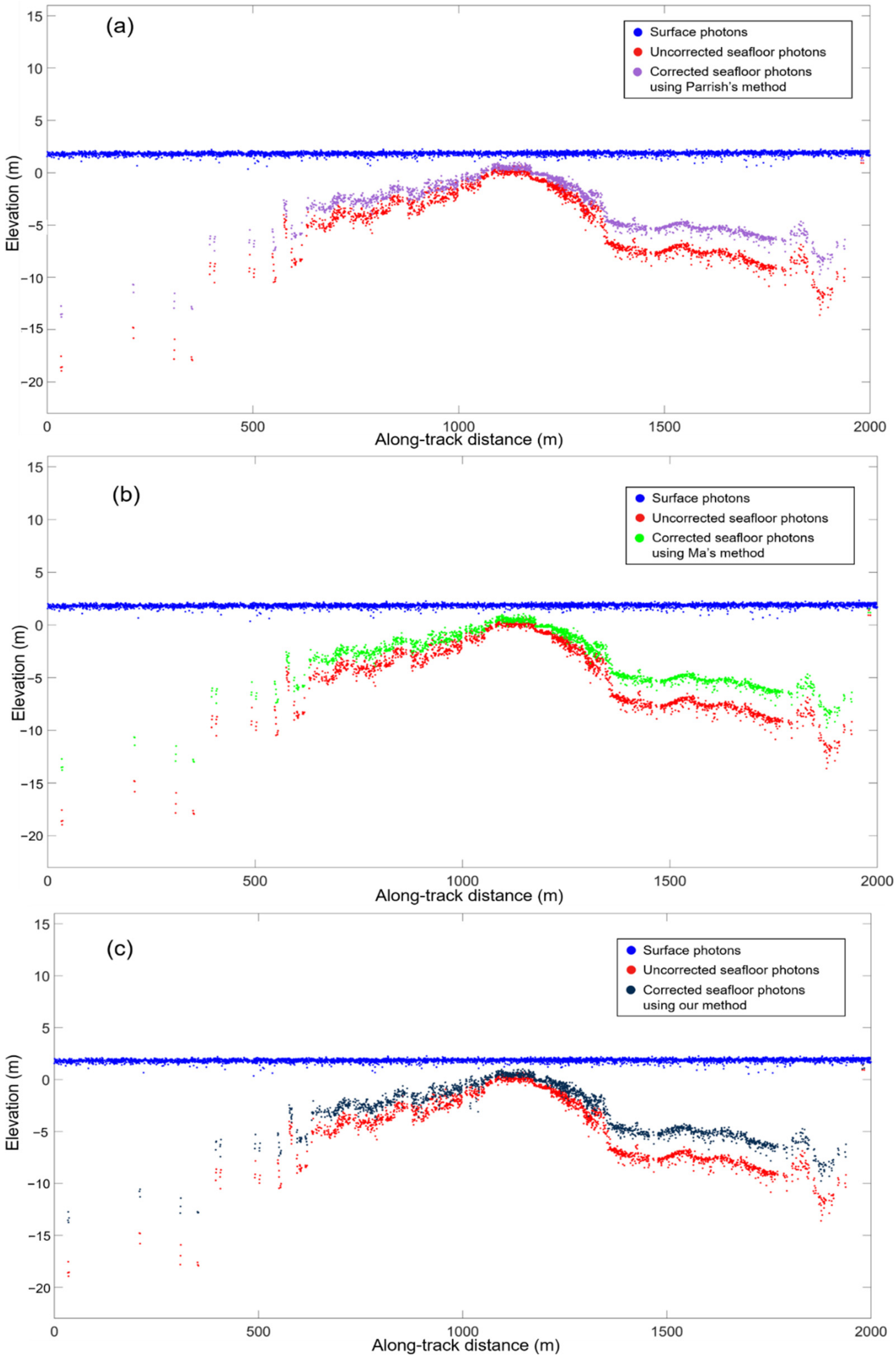

Figure 4. Photon results from different refraction-corrected methods between Quanfu Island and Yinyu Island. Using the separated seafloor and surface signal photons, we obtained three results: the seafloor points corrected using (**a**) Parrish's method, (**b**) Ma's method, and (**c**) our method. In the figure, the surface and seafloor points are shown in blue and red, respectively.

3.2. Processing Results of Sentinel-2

In this study, Hedley's method was used to remove the sunglint component of the remotely sensed signal from visible-wavelength spectral bands. The image used for the de-glinting was obtained after water bodies extraction (shown in Figure 5a).

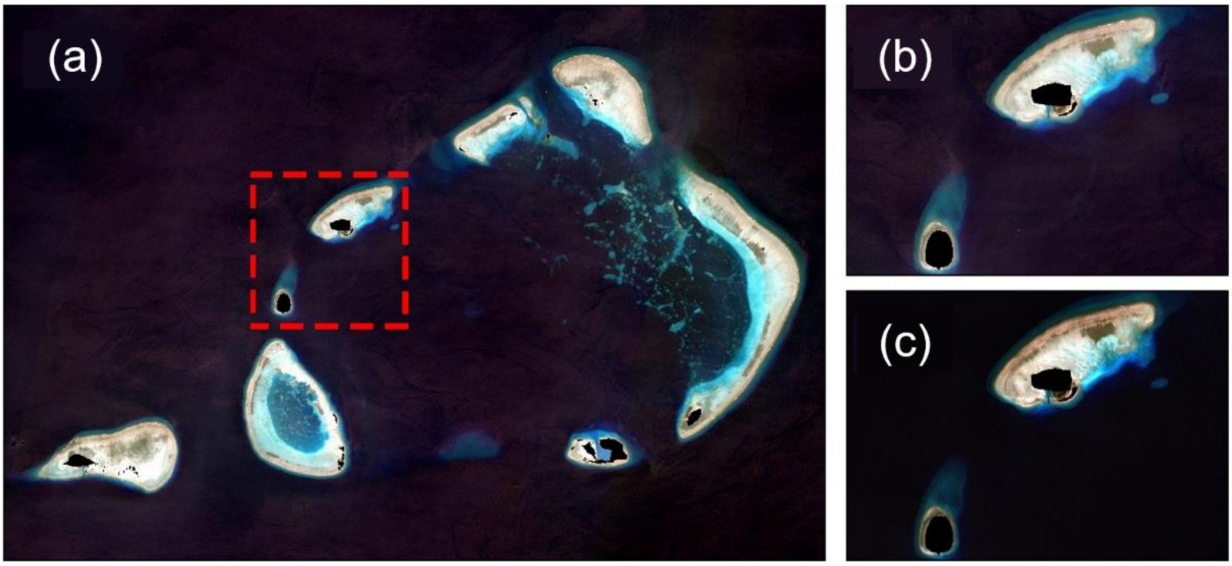

Figure 5. (**a**) The sunglint in the Sentinel-2 L2A image around the Yongle Atoll. Panels (**b**,**c**) present the images before and after de-glinting near Ganquan Island and Shanhu Island, respectively. Compared with (**b**), there are no noticeable white stripes or bright spots in (**c**).

The area shown in the red box of Figure 5a includes Ganquan Island and Shanhu Island, and the comparison before and after de-glinting is shown in Figure 5b,c.

Figure 5a features many sunglints in the image. The area shown in the red box in Figure 5a is Ganquan Island, and many white stripes are apparent in nearshore environments before de-glinting. Compared with Figure 5b, the effect after de-glinting is displayed in Figure 5c. The white stripes are reduced, the image is clearer, and the effect of sunglint removal is good. After de-glinting, the image can be used in bathymetric modeling and retrieval.

The refraction-corrected seafloor photons and flare-corrected multispectral data were fed into the band ratios model; the linear band model and the band ratio model were retrained. The gross errors were discarded according to the three-sigma criteria to ensure the reliability of the model. Next, 70% of the samples were used for modeling. The remaining samples were devoted to model testing, which was dedicated to testing model errors and was not included in the modeling training. The maximum water depth of the model was set to 18 m, which combined the ICESat-2 bathymetric performance and the applicable range of the SDB method. When the depth was greater than the threshold, the inversion error increased, and the reference significance was poor.

3.3. Results of the SDB Method

We applied the trained parameters of the band ratio model to the whole area and obtained the bathymetric map of Yongle Atoll (Figure 6) and Ganquan Island (Figure 7). In the vicinity of Ganquan Island, the orange box in Figure 1, the accuracy of the bathymetric maps obtained was verified using in-situ data. Figures 7–9 elaborate on the results and parameters of each model. In Figure 7, the spatial distributions of the in-situ points (Figure 7a) and bathymetric maps derived (Figure 7b–e) near Ganquan Island are illustrated. To further verify the accuracy of the estimation results, the error scatter diagram, R2, RMSE, the regression line, and the regression equation between the retrieved water depths and in-situ depths near Ganquan Island are illustrated in Figure 8. Similarly, the normalized residual results, the means, and the standard deviations of the four methods are displayed in Figure 9. In Figure 8, for bathymetric points acquired using the four methods, the R2 are from 0.79 to 0.86 with a mean of 0.81, and the training RMSE (Root Mean Squared Error) are from 1.48 m to 1.99 m with a mean of 1.69 m. The RMSE and R2 of Figure 8a are worse than those of the other models, with a systematic bias (Figure 9a demonstrates that their residuals do not conform to a normal distribution). These indicate that an accurate water depth can be detected using our refraction correction method. Generally, our method achieves better results compared to the other three methods in the Yongle Atoll.

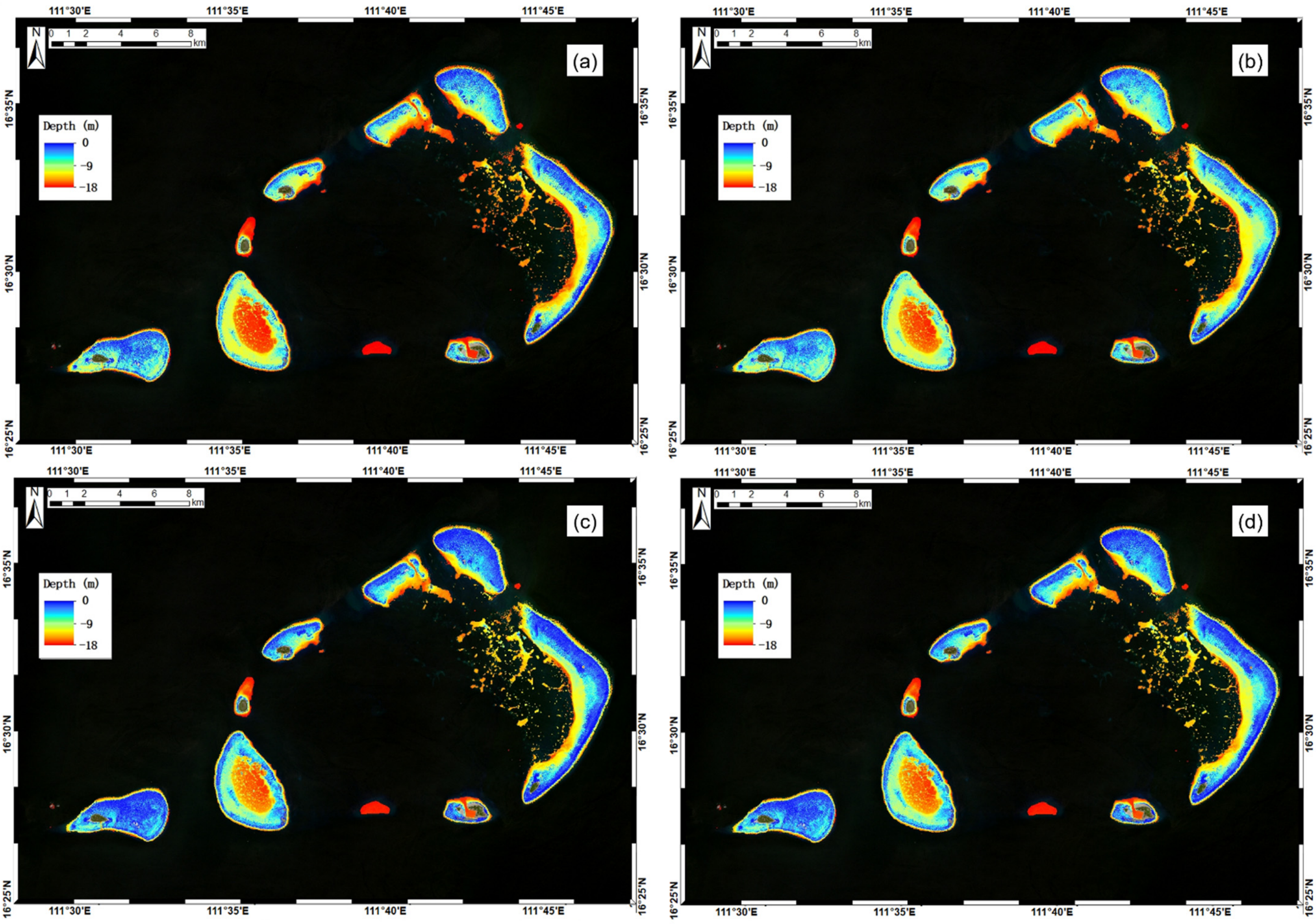

Figure 6. Bathymetric maps of the Yongle Atoll. Maps with seafloor points (**a**) uncorrected, (**b**) corrected using Parrish's method, (**c**) corrected using Ma's method, and (**d**) corrected using our method. Panels (**a**–**d**) feature the same scale bars and color bars.

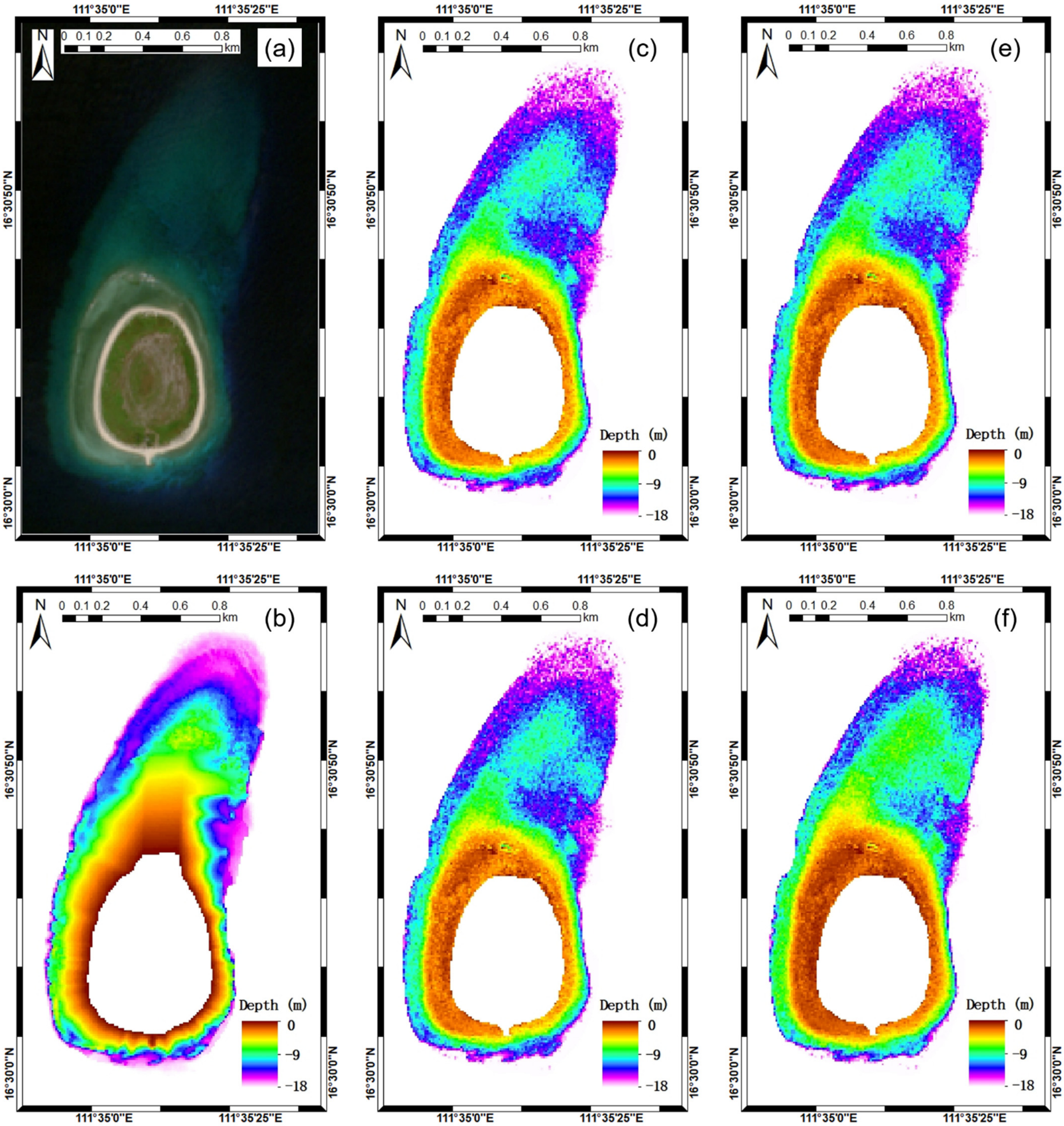

Figure 7. Bathymetric maps near Ganquan Island. (**a**) Sentinel-2 imagery of Ganquan Island. Maps with (**b**) in-situ data, (**c**) uncorrected seafloor points, (**d**) seafloor points corrected using Parrish's method, (**e**) seafloor points corrected using Ma's method, and (**f**) seafloor points corrected using our method. Panels (**a**–**f**) have the same scale bars and color bars.

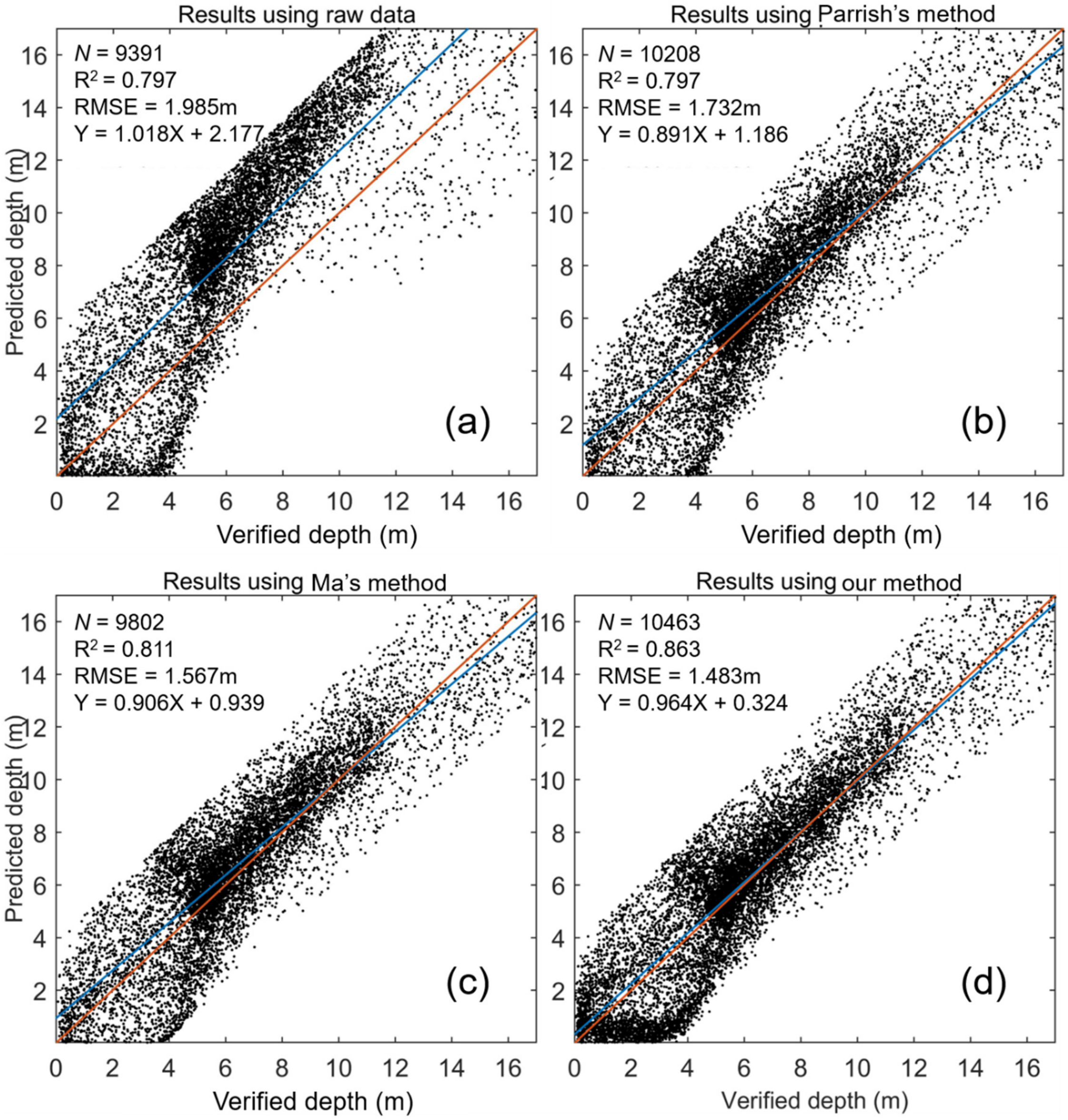

Figure 8. Error scatter diagrams of derived water depths and in-situ depths at Ganquan Island. The retrieved water depths were obtained from different seafloor points: (**a**) uncorrected, (**b**) corrected using Parrish's method, (**c**) corrected using Ma's method, and (**d**) corrected using our method. The red line is the 1:1 line, whereas the blue line corresponds to the regression line. *N* is the number of in-situ points used to validate the retrieved bathymetric maps, with gross errors already discarded. The regression equations of the different models are also included.

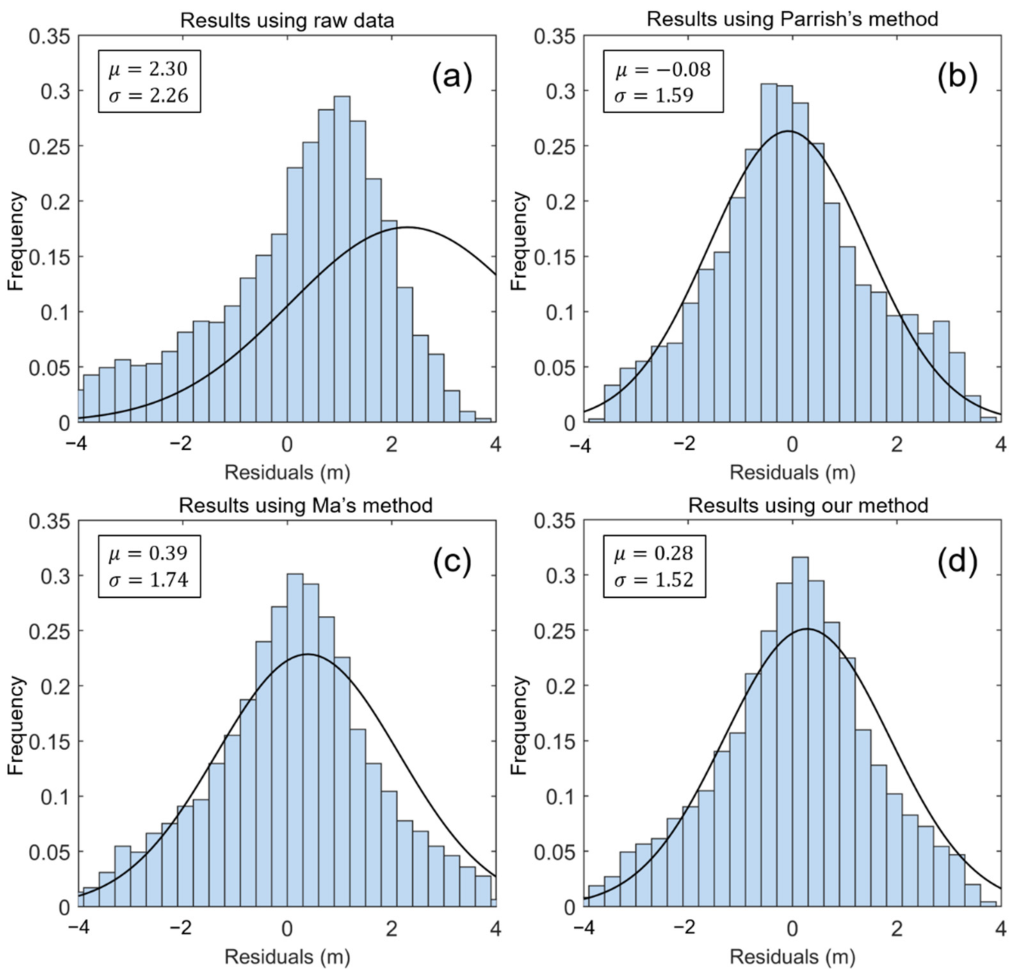

Figure 9. Normalized residual results of derived water depths and in-situ depths at Ganquan Island. As in Figure 8, the retrieved water depths were obtained from different seafloor points: (**a**) uncorrected, (**b**) corrected using Parrish's method, (c) corrected using Ma's method, and (**d**) corrected using our method.

4. Discussions

4.1. Error Analyses of Underwater Photon Position

The photon localization of ICESat-2 is a complex procedure influenced by several factors, which can cause various errors. The causes of the positioning errors of land photons, such as satellite clock difference, satellite orbit error, and atmospheric delay error, have been discussed and corrected in detail. Through rigorous correction, photon coordinates can be obtained accurately. However, to date, no exhaustive investigations have focused on underwater photon positioning errors. Unlike surface or land photons, underwater photons penetrate the water column and are thus affected by other factors [19,33]. We classify the errors as follows.

The primary error is caused by the change in the propagation medium. A 532-nm laser beam features different refraction indices in seawater and air, causing changes in propagation speed and direction. The nonvertical incidence of the laser beam (as in the vast majority of cases) is refracted at the air–seawater intersection, which satisfies Snell's law [38]. The second error refers to that arising from the current sea surface. The dynamic fluctuations and slope of the sea surface, caused by natural effects such as wind, waves, and tides, make it difficult to calculate the incidence angle and underwater distance accurately. Finally, underwater photons cannot find their corresponding incident point coordinates precisely because of the lack of signal waveform information in photon-counting lidars. This also introduces errors.

Overall, each error consistently makes the corrected photon water depth shallower. For example, assume a seafloor photon with a 20 m water depth corrected by Snell's law, an incidence angle of 8°, and a sea-surface fluctuation of 0.5 m. The above errors will offset the photon by 2.07 m in the x-direction and by 0.61 m in the z-direction, with positive values indicating the direction along the coordinate axis of Figure 2. When the vertical accuracy requirement is not particularly high, the actual depth can be three-quarters of the uncorrected bathymetry. As the footprint of the ICESat-2 spot is 17 m, all the corrections to the horizontal direction can reasonably be ignored.

4.2. Potential Contributions and Limitations

The dataset in this study can benefit multiple applications across disciplines. First, ATLAS features the ability to acquire lake bathymetry over small areas because of its improved along-track sampling interval (0.7 m), footprint diameter (17 m), and horizontal track spacing (narrowed to 2 km or less), which make it suitable for water estimations over regionally dispersed areas [39]. The unique signal permeability of ICESat-2 makes it suitable for studies in land–water interaction zones (e.g., Venice and Hawaii), which reduces coordinate system conversion errors compared with those of traditional land–water separation measurements [40,41]. Second, with the increasing density of the ICESat-2 data, we can explore the global variability of lake water and deepen our understanding of the water cycle. In addition, the SDB method, combined with multispectral and ICESat-2 data, is not only applicable to shallow seas and areas around islands; it is also essential for hard-to-reach inland waters. The method can obtain high-precision regional bathymetry values without in-situ measurements. This is beneficial for the conservation of ecological diversity and is of significance for ecologically fragile areas, such as plateau lakes. In the future, using ICESat-2 in combination with the to-be-launched Surface Water and Ocean Topography mission satellite, global water bodies can be further probed, providing a comprehensive global capability for bathymetric mapping.

The method proposed in the paper features a few limitations. First, the measured depth of the method is influenced by the water clarity. Parrish analyzed the ATLAS's depth penetration capability using Visible Infrared Imaging Radiometer Suite (VIIRS) Kd (490) data for four project sites, and found that the maximum depth mapping performance of ATLAS was nearly 1 Secchi in depth [20]. In case II water areas, the maximum depth of bathymetry derived from ICESat-2 is limited. Second, the method is not applicable to non-shallow water areas. The satellite-derived bathymetry method is only applicable to shallow water areas such as around islands and coastal zones. The accuracy of projected bathymetry declines when the detected water depth exceeds 20 m, which can reduce the availability of data.

5. Conclusions

In this study, we developed a refraction correction method taking into account sea-surface undulation to produce accurate bathymetric photons and mapped the bathymetry pattern of the Yongle Atoll by coupling high-precision photons from ICESat-2 and high-resolution Sentinel satellite imagery. Various refraction correction methods were used to compare the airborne LiDAR bathymetry data to verify the correctness and reliability of our novel method. The experimental results illustrate that the proposed refraction correction method could efficiently improve the accuracy of nearshore bathymetry with an RMSE of 1.48 m and R2 of 0.86. These provide important evidence of the reliability of ICESat-2's bathymetric performance in the case of Ganquan Island. The weaker performance of the bathymetry results using uncorrected photons showed that subsequent corrections of the raw seafloor data could positively contribute to the accurate prediction of water depth. However, there is no area with both in-situ measurements and ICESat-2 trajectories because of a lack of data. In our future research, we will devote ourselves to finding an ideal study area in which to evaluate refraction correction directly. In the future, we will quickly and accurately acquire underwater topographic features in shallow-water areas using the underwater signal points of ICESat-2 and massive multispectral data using the SDB method.

Author Contributions: Conceptualization, C.L.; methodology, C.L.; software, C.L.; validation, C.L. and J.Q.; formal analysis, J.Q.; investigation, C.L. and W.X.; data curation, C.L. and J.Q.; writing—original draft preparation, C.L., W.M. and Q.T.; writing—review and editing, J.L., W.X. and X.Z.; visualization, J.Q. and W.M.; supervision, J.L. and Q.T.; project administration, J.L.; funding acquisition, J.L. All authors have read and agreed to the published version of the manuscript.

Funding: This research is supported by the National Natural Science Foundation of China (41871381, 41876111, 41401537); National Key Research and Development Program of China (2018YFC0309901); Chinese Arctic and Antarctic Administration Project (IRASCC 2020-2022).

Acknowledgments: We thank the NASA NSIDC for distributing the ICESat-2 data; the European Space Agency (ESA) for distributing the Sentinel-2 imagery. Furthermore, we thank the anonymous reviewers and members of the editorial team for their constructive comments.

Conflicts of Interest: The authors declare that they have no known competing financial interests or personal relationships that could appear to influence the work reported in this paper.

References

1. Mancini, S.; Olsen, R.C.; Abileah, R.; Lee, K.R. Automating nearshore bathymetry extraction from wave motion in satellite optical imagery. *SPIE Proc.* **2012**, *8390*, 83900P.
2. Moore, L.J. Shoreline mapping techniques. *J. Coast. Res.* **2000**, *16*, 111–124.
3. Amiri-Simkooei, A.; Snellen, M.; Simons, D.G. Riverbed sediment classification using multi-beam echo-sounder backscatter data. *J. Acoust. Soc. Am.* **2009**, *126*, 1724. [CrossRef]
4. Kogut, T.; Bakuła, K. Improvement of Full Waveform Airborne Laser Bathymetry Data Processing based on Waves of Neighborhood Points. *Remote Sens.* **2019**, *11*, 1255. [CrossRef]
5. Zhang, K.; Yang, F.; Zhang, H.; Su, D.; Li, Q. Morphological characterization of coral reefs by combining lidar and MBES data: A case study from Yuanzhi Island, South China Sea. *J. Geophys. Res. Oceans* **2017**, *122*, 4779–4790. [CrossRef]
6. Armon, M.; Dente, E.; Shmilovitz, Y.; Mushkin, A.; Cohen, T.J.; Morin, E.; Enzel, Y. Determining Bathymetry of Shallow and Ephemeral Desert Lakes Using Satellite Imagery and Altimetry. *Geophys. Res. Lett.* **2020**, *47*, e2020GL087367. [CrossRef]
7. Dierssen, H.M.; Zimmerman, R.C.; Leathers, R.A.; Downes, T.V.; Davis, C.O. Ocean color remote sensing of seagrass and bathymetry in the Bahamas Banks by high-resolution airborne imagery. *Limnol. Oceanogr.* **2003**, *48*, 444–455. [CrossRef]
8. Sagawa, T.; Yamashita, Y.; Okumura, T.; Yamanokuchi, T. Satellite Derived Bathymetry Using Machine Learning and Multi-Temporal Satellite Images. *Remote Sens.* **2019**, *11*, 1155. [CrossRef]
9. Duplančić Leder, T.; Leder, N.; Peroš, J. Satellite Derived Bathymetry Survey Method—Example of Hramina Bay. *Trans. Marit. Sci.* **2019**, *8*, 99–108. [CrossRef]
10. Thomas, N.; Pertiwi, A.P.; Traganos, D.; Lagomasino, D.; Poursanidis, D.; Moreno, S.; Fatoyinbo, L. Space-Borne Cloud-Native Satellite-Derived Bathymetry (SDB) Models Using ICESat-2 And Sentinel-2. *Geophys. Res. Lett.* **2021**, *48*, e2020G–e92170G. [CrossRef]
11. Vinayaraj, P. Development of Algorithms for Near-shore Satellite Derived Bathymetry Using Multispectral Remote Sensing Images. Ph.D. Thesis, Osaka City University, Osaka, Japan, 2019. Available online: http://dlisv03.media.osaka-cu.ac.jp/contents (accessed on 21 July 2021).
12. Lyzenga, D.R. Passive remote sensing techniques for mapping water depth and bottom features. *Appl. Opt.* **1978**, *17*, 379–383. [CrossRef] [PubMed]
13. Lyzenga, D.R. Remote sensing of bottom reflectance and water attenuation parameters in shallow water using aircraft and Landsat data. *Int. J. Remote Sens.* **1981**, *2*, 71–82. [CrossRef]
14. Stumpf, R.P.; Holderied, K.; Sinclair, M. Determination of water depth with high-resolution satellite imagery over variable bottom types. *Limnol. Oceanogr.* **2003**, *48*, 547–556. [CrossRef]
15. Poursanidis, D.; Traganos, D.; Chrysoulakis, N.; Reinartz, P. Cubesats Allow High Spatiotemporal Estimates of Satellite-Derived Bathymetry. *Remote Sens.* **2019**, *11*, 1299. [CrossRef]
16. Hsu, H.J.; Huang, C.Y.; Jasinski, M.; Li, Y.; Gao, H.; Yamanokuchi, T.; Wang, C.G.; Chang, T.M.; Ren, H.; Kuo, C.Y.; et al. A semi-empirical scheme for bathymetric mapping in shallow water by ICESat-2 and Sentinel-2: A case study in the South China Sea. *ISPRS J. Photogramm.* **2021**, *178*, 1–19. [CrossRef]
17. Markus, T.; Neumann, T.; Martino, A.; Abdalati, W.; Brunt, K.; Csatho, B.; Farrell, S.; Fricker, H.; Gardner, A.; Harding, D.; et al. The Ice, Cloud, and land Elevation Satellite-2 (ICESat-2): Science requirements, concept, and implementation. *Remote Sens. Environ.* **2017**, *190*, 260–273. [CrossRef]

18. Neumann, T.A.; Martino, A.J.; Markus, T.; Bae, S.; Bock, M.R.; Brenner, A.C.; Brunt, K.M.; Cavanaugh, J.; Fernandes, S.T.; Hancock, D.W.; et al. The Ice, Cloud, and Land Elevation Satellite-2 mission: A global geolocated photon product derived from the Advanced Topographic Laser Altimeter System. *Remote Sens. Environ.* **2019**, *233*, 111325. [CrossRef] [PubMed]
19. Fang, Y.; Cao, B.; Gao, L.; Hu, H.; Jiang, Z. Development and application of lidar mapping satellite. *Hongwai Yu Jiguang Gongcheng/Infrared Laser Eng.* **2020**, *49*, 20201044-1.
20. Parrish, C.E.; Magruder, L.A.; Neuenschwander, A.L.; Forfinski-Sarkozi, N.; Alonzo, M.; Jasinski, M. Validation of ICESat-2 ATLAS Bathymetry and Analysis of ATLAS's Bathymetric Mapping Performance. *Remote Sens.* **2019**, *11*, 1634. [CrossRef]
21. Zhang, W.; Xu, N.; Ma, Y.; Yang, B.; Zhang, Z.; Wang, X.H.; Li, S. A maximum bathymetric depth model to simulate satellite photon-counting lidar performance. *Isprs J. Photogramm.* **2021**, *174*, 182–197. [CrossRef]
22. Zhang, Z.; Liu, X.; Ma, Y.; Xu, N.; Zhang, W.; Li, S. Signal Photon Extraction Method for Weak Beam Data of ICESat-2 Using Information Provided by Strong Beam Data in Mountainous Areas. *Remote Sens.* **2021**, *13*, 863.
23. Cao, B.; Fang, Y.; Gao, L.; Hu, H.; Jiang, Z.; Sun, B.; Lou, L. An active-passive fusion strategy and accuracy evaluation for shallow water bathymetry based on ICESat-2 ATLAS laser point cloud and satellite remote sensing imagery. *Int. J. Remote Sens.* **2021**, *42*, 2783–2806. [CrossRef]
24. Popescu, S.C.; Zhou, T.; Nelson, R.; Neuenschwander, A.; Sheridan, R.; Narine, L.; Walsh, K.M. Photon counting LiDAR: An adaptive ground and canopy height retrieval algorithm for ICESat-2 data. *Remote Sens. Environ.* **2018**, *208*, 154–170. [CrossRef]
25. Chen, Y.; Le, Y.; Zhang, D.; Wang, Y.; Qiu, Z.; Wang, L. A photon-counting LiDAR bathymetric method based on adaptive variable ellipse filtering. *Remote Sens. Environ.* **2021**, *256*, 112326. [CrossRef]
26. Xu, N.; Ma, Y.; Zhang, W.; Wang, X.H.; Yang, F.; Su, D. Monitoring Annual Changes of Lake Water Levels and Volumes over 1984–2018 Using Landsat Imagery and ICESat-2 Data. *Remote Sens.* **2020**, *12*, 4004. [CrossRef]
27. Ma, Y.; Xu, N.; Liu, Z.; Yang, B.; Yang, F.; Wang, X.H.; Li, S. Satellite-derived bathymetry using the ICESat-2 lidar and Sentinel-2 imagery datasets. *Remote Sens. Environ.* **2020**, *250*, 112047. [CrossRef]
28. Ma, Y.; Xu, N.; Sun, J.; Wang, X.H.; Yang, F.; Li, S. Estimating water levels and volumes of lakes dated back to the 1980s using Landsat imagery and photon-counting lidar datasets. *Remote Sens. Environ.* **2019**, *232*, 111287. [CrossRef]
29. Chen, Y.; Zhu, Z.; Le, Y.; Qiu, Z.; Chen, G.; Wang, L. Refraction correction and coordinate displacement compensation in nearshore bathymetry using ICESat-2 lidar data and remote-sensing images. *Opt. Express* **2021**, *29*, 2411. [CrossRef]
30. Drusch, M.; Del Bello, U.; Carlier, S.; Colin, O.; Fernandez, V.; Gascon, F.; Hoersch, B.; Isola, C.; Laberinti, P.; Martimort, P.; et al. Sentinel-2: ESA's Optical High-Resolution Mission for GMES Operational Services. *Remote Sens. Environ.* **2012**, *120*, 25–36. [CrossRef]
31. Ester, M.; Kriegel, H.; Sander, J.; Xu, X. A density-based algorithm for discovering clusters in large spatial databases with noise. *Kdd* **1996**, *96*, 226–231.
32. Forfinski-Sarkozi, N.; Parrish, C. Analysis of MABEL Bathymetry in Keweenaw Bay and Implications for ICESat-2 ATLAS. *Remote Sens.* **2016**, *8*, 772. [CrossRef]
33. Neuenschwander, A.; Magruder, L. The Potential Impact of Vertical Sampling Uncertainty on ICESat-2/ATLAS Terrain and Canopy Height Retrievals for Multiple Ecosystems. *Remote Sens.* **2016**, *8*, 1039. [CrossRef]
34. Vernimmen, R.; Hooijer, A.; Pronk, M. New ICESat-2 Satellite LiDAR Data Allow First Global Lowland DTM Suitable for Accurate Coastal Flood Risk Assessment. *Remote Sens.* **2020**, *12*, 2827. [CrossRef]
35. Thomas, T.C.; Luthcke, S.B.; Pennington, T.A.; Nicholas, J.B.; Rowlands, D.D. ICESat-2 Precision Orbit Determination. *Earth Space Sci.* **2021**, *8*, e2020EA001496. [CrossRef]
36. Padman, L.; Erofeeva, S. Tide model driver (TMD) manual. *Earth Space Res.* **2005**. Available online: https://svn.oss.deltares.nl/repos/openearthtools/trunk/matlab/applications/DelftDashBoard/utils/tmd/Documentation/README_TMD_vs1.2.pdf (accessed on 21 July 2021).
37. Hedley, J.D.; Harborne, A.R.; Mumby, P.J. Technical note: Simple and robust removal of sun glint for mapping shallow-water benthos. *Int. J. Remote Sens.* **2007**, *26*, 2107–2112. [CrossRef]
38. Yuan, C.; Gong, P.; Bai, Y. Performance assessment of ICESat-2 laser altimeter data for water-level measurement over lakes and reservoirs in China. *Remote Sens.* **2020**, *12*, 770. [CrossRef]
39. Li, Y.; Gao, H.; Zhao, G.; Tseng, K. A high-resolution bathymetry dataset for global reservoirs using multi-source satellite imagery and altimetry. *Remote Sens. Environ.* **2020**, *244*, 111831. [CrossRef]
40. Gao, J. Bathymetric mapping by means of remote sensing: Methods, accuracy and limitations. *Prog. Phys. Geogr. Earth Environ.* **2009**, *33*, 103–116. [CrossRef]
41. Li, Y.; Gao, H.; Jasinski, M.F.; Zhang, S.; Stoll, J.D. Deriving high-resolution reservoir bathymetry from ICESat-2 prototype photon-counting lidar and landsat imagery. *IEEE Trans. Geosci. Remote Sens.* **2019**, *57*, 7883–7893. [CrossRef]